Journal of Catalysis **181,** 57–72 (1999)
Article ID jcat.1998.2269, available online at http://www.idealibrary.com on IDEAL®

Structural and Catalytic Characterization of Solid Acids Based on Zirconia Modified by Tungsten Oxide

David G. Barton,* Stuart L. Soled,† George D. Meitzner,‡ Gustavo A. Fuentes,§ and Enrique Iglesia*,[1]

*Department of Chemical Engineering, University of California at Berkeley, Berkeley, California 94720; †Corporate Research Laboratory, Exxon Research and Engineering, Route 22 East, Annandale, New Jersey 08801; ‡Edge Analytical, Inc., 2126 Allen Blvd., Middleton, Wisconsin 53562; and §Departamento de Ingenieria de Procesos, Universidad Autonoma Metropolitana-Iztapalapa, A.P. 55-534, 09340 Mexico, D.F., Mexico

Received February 2, 1998; revised August 28, 1998; accepted August 31, 1998

Tungsten oxide species form strong acid sites on ZrO_2 supports and inhibit ZrO_2 crystallite sintering and tetragonal to monoclinic structural transformations. W-L_I X-ray absorption near-edge spectra suggest that the W centers are in a distorted octahedral oxygen environment, even after dehydration at 673 K, in all WO_x–ZrO_2 samples (2–21 wt.% W) oxidized at 1073 K. Maximum *o*-xylene isomerization turnover rates (per W atom) on WO_x–ZrO_2 solids occur at WO_x surface densities (10 W nm^{-2}) that exceed the theoretical monolayer capacity of ZrO_2. Similar turnover rates are obtained on WO_x–ZrO_2 samples with similar WO_x surface densities (W nm^{-2}) over a large range of oxidation temperatures (773–1223 K) and WO_x concentrations (5–21 wt.% W). UV–visible spectra suggest an increase in WO_x domain size with increasing surface density. High isomerization turnover rates appear to require the presence of WO_x domains of intermediate size on ZrO_2 surfaces. WO_x domains of intermediate size appear to provide a compromise between reducibility and accessibility of WO_x centers. These domains are necessary to delocalize a temporary charge imbalance that forms Brønsted acid sites in the presence of H_2 and stabilizes carbocation intermediates. The presence of H_2 during *o*-xylene isomerization increases turnover rates and prevents rapid deactivation. Slow D_2/*o*-xylene exchange reactions indicate that H atoms from H_2 are not frequently involved in the activation or desorption of xylenes. H_2 is required, however, in order to reverse the occasional desorption of H atoms during *o*-xylene isomerization reactions. These desorption processes lead to the destruction of Brønsted acid sites by the formation of strongly adsorbed unsaturated species in the absence of H_2. After promotion with Pt (0.3 wt.%), WO_x–ZrO_2 solids catalyze *n*-heptane isomerization in the presence of H_2 at 400–500 K with much higher selectivity than sulfated oxides or zeolitic acids at similar turnover rates. On Pt/WO_x–ZrO_2, efficient hydrogen transfer steps prevent extensive cracking of adsorbed carbocations by limiting their surface lifetimes.

BACKGROUND

Current catalytic processes for alkane isomerization and alkylation require liquid acids (e.g., H_2SO_4, HF, $AlCl_3$) or halogen-promoted metal oxides (e.g., Cl–Al_2O_3), which pose significant containment, corrosion, and environmental challenges (1). These problems can be circumvented by the development of strong solid acid catalysts consisting of metal oxides. The development of solid acids that are stable, regenerable, and active at the low temperatures required for favorable isomerization thermodynamics remains a formidable challenge.

Recently, metal oxides promoted by sulfur compounds have been studied as strong solid acid catalysts (2, 3), especially SO_x- promoted zirconia (4) containing iron or manganese oxides as promoters (5) or noble metals to inhibit deactivation (6–8). Yet, their low isomerization selectivity for C_{7+} alkanes, their poor stability, and their tendency to form volatile sulfur compounds during catalysis and regeneration limit their applicability in isomerization and alkylation processes.

Tungsten oxide-based materials comprise another interesting class of solid acids. The small and highly charged W^{+6} cations are found in several solid acids: heteropolyoxoanion compounds, such as 12-tungstophosphoric acid (9), oxygen-modified tungsten carbides (10), and WO_x dispersed on γ-Al_2O_3 (11) and ZrO_2 (12–19). This paper focuses on WO_x dispersed on ZrO_2 (WO_x–ZrO_2), first reported to be strongly acidic by Hino and Arata (20). These authors suggested, based on color changes by Hammett indicators, that acid sites stronger than 100% sulfuric acid may exist ($H_0 \leq -14.52$), but the use of this technique as a measure of acid strength on solids is generally unreliable (21). Butene dimerization studies have confirmed that acid sites on WO_x–ZrO_2 have catalytic activity comparable to those on SO_x–ZrO_2 (14). Hino and Arata (12) reported low-temperature catalytic activity for *n*-pentane and *n*-hexane isomerization, but cracking selectivities were very high (>50%) even at low conversion. The addition of a

[1] To whom correspondence should be addressed. Fax: (510) 642-4778. E-mail: iglesia@cchem.berkeley.edu.

0021-9517/99 $30.00

metal component (<1% wt. Pt) to WO_x–ZrO_2 catalysts and the presence of H_2 resulted in very active and selective catalysts for *n*-alkane isomerization (16–18, 22) and cycloalkane ring-opening (15) reactions with excellent stability and high selectivity to isomers.

Acid-catalyzed alkane isomerization has become increasingly important in the synthesis of high-octane blending components and lubricant basestocks. Currently, isomerization of heptane and larger alkanes (C_{7+}) is limited by high selectivity to cracking products and by poor yields of high-octane multibranched alkanes containing quaternary carbons. Long carbocation surface residence times during C_{7+} alkane isomerization and cracking pathways that directly form stable *tert*-butyl surface carbocations favor cracking reactions on strong acids (23). In practice, undesired cracking reactions limit paraffin isomerization processes to C_4–C_6 alkanes.

Iglesia *et al*. (24) have shown that high isomerization selectivity (>70%) in *n*-heptane reactions can be obtained on oxygen-modified tungsten carbide catalysts at high temperatures (~623 K). These catalysts behave as bifunctional metal–acid catalysts with a WC dehydrogenation function and a WO_x acid function, but they require high temperatures (~623 K), which favor hydrogenolysis pathways and monobranched isoheptanes. In another study, Iglesia *et al*. (6) reported *n*-heptane isomerization results at lower temperatures (473 K) on a stronger acid (Pt/SO_x–ZrO_2). They found predominately isobutane and propane among cracking products (~50% total cracking selectivity at low conversions ~10%), consistent with acid-catalyzed cracking of heptyl cations. The addition of hydride transfer cocatalysts showed that slow hydride transfer to surface carbocations limits isomerization rates and leads to long carbocation surface lifetimes and high cracking selectivity (6). These studies along with Hino and Arata's discovery of the unique properties of WO_x–ZrO_2 led us to study the synthesis and characterization of these catalysts promoted by Pt for *n*-heptane isomerization reactions (Pt/WO_x–ZrO_2). This catalyst promoted by Pt couples a strong acid component active at low temperatures with clean noble metal particles that increase hydride transfer rates (18). Here, we examine the structural stabilization of the zirconia support and the nature of the surface WO_x groups. We also probe the effects of H_2 on *n*-heptane and *o*-xylene isomerization, and use the turnover rates for the "monofunctional" isomerization of *o*-xylene in order to compare WO_x–ZrO_2 samples with a wide range of WO_x surface densities.

EXPERIMENTAL

Synthesis of WO_x–ZrO_2 Catalytic Solids

WO_x–ZrO_2 samples were prepared by incipient wetness impregnation of zirconium oxyhydroxide ($ZrO_x(OH)_{4-2x, x<2}$) solids with ammonium metatungstate solutions. High-surface-area $ZrO_x(OH)_{4-2x}$ was prepared by hydrolysis of a 0.5 M zirconyl chloride solution ($ZrOCl_2 \cdot 8H_2O$, Aldrich, >98 wt.%, Hf <0.5 wt.%, 500 $cm^3\ h^{-1}$ feed) using the controlled addition of NH_4OH (14.8 N) to obtain a constant pH of 10. This pH was chosen based on previous studies (25–27), in which the mesoporosity, surface area, and total pore volume of $ZrO_x(OH)_{4-2x}$ were shown to increase with increasing precipitation pH. The precipitate was immediately filtered and washed repeatedly by redispersion in a NH_4OH solution (pH 10) in order to remove residual chloride. After each wash, a couple of drops of a 3 M $AgNO_3$ solution were added to the filtrate liquid until it showed no visible signs of AgCl formation (<10 ppm residual Cl^-). The $ZrO_x(OH)_{4-2x}$ gel was dried at 383 K overnight, crushed, and sieved to retain particles with 0.12–0.38 mm diameter.

The dried particles were impregnated to the point of incipient wetness (0.29 cm^3 H_2O per 1.0 g $ZrO_x(OH)_{4-2x}$) with ammonium metatungstate ($(NH_4)_6H_2W_{12}O_{40}$, Strem Chemicals, 99.9%) solutions to give 2–21 wt.% W after oxidation treatments. The impregnated samples were dried at 383 K overnight and oxidized in flowing dry air at temperatures between 773 and 1273 K. All samples were oxidized in shallow quartz boats inside a 25-mm-diameter quartz tube with flowing air (Linde Zero Grade, 3.3 $cm^3\ s^{-1}$), dried and purified with Drierite and 13X molecular sieve traps. The samples were heated at a rate of 0.167 K s^{-1} to the final temperature (measured in a quartz thermowell just above the sample bed), held for 3 h, and cooled to room temperature in flowing air. After oxidation at 1073 K, a portion of the sample containing 12 wt.% W was impregnated to the point of incipient wetness with a solution of tetra-amine platinum hydroxide (Degussa), dried at 383 K overnight, and oxidized for 3 h at 723 K (0.3 wt.% Pt). Nominal tungsten and platinum contents (after oxidative treatments) were based on precursor decomposition weight losses obtained from thermogravimetric analysis.

Chemisorption and Physisorption Measurements

Chemisorption data were collected on a Quantachrome 1C Autosorb apparatus. Samples were dried in a box furnace at 723 K in air immediately before loading. Pt/WO_x–ZrO_2 samples were heated in H_2 at 0.033 K s^{-1} to the final reduction temperature (either 473 or 823 K) and held isothermally for 1 h. After evacuation, the samples were cooled to 313 K, and an 11-point H_2 adsorption isotherm was obtained between 2.7 and 53 kPa. The linear portion of the isotherm was extrapolated to zero pressure to obtain the combined (total) uptake. After evacuation at 313 K, the isotherm was again measured; the linear portion was extrapolated to zero pressure to obtain the weakly adsorbed fraction of the total initial uptake, and the strong chemisorption uptake was obtained by difference. After this measurement,

the catalyst was again reduced at the original reduction temperature, and oxygen uptakes were obtained at 313 K. CO uptakes at 313 K were measured on a fresh sample pretreated as described above. A similar procedure was used to determine reversible H_2 chemisorption uptakes at 523 K on WO_x–ZrO_2 samples (without Pt) reduced at 523 K, except the uptakes are reported at 45 kPa H_2, which results in a better estimate of the amount of reactive surface H species present during reaction.

Physical surface areas were obtained by N_2 physisorption using a Quantasorb surface area analyzer (Quantachrome Corporation) and a standard multipoint BET isotherm (28). Samples previously oxidized at high temperatures (>473 K) were degassed in flowing N_2 for 1 h at 473 K; other samples were degassed for 3 h at 383 K before N_2 physisorption measurements.

Powder X-Ray Diffraction Measurements

X-ray powder diffraction (XRD) patterns were recorded using a Siemens D5000 Diffractometer with Cu$K\alpha$ radiation and a scanning rate of 0.002° s^{-1}. These patterns were used to quantify the relative amounts and crystallite sizes of each ZrO_2 phase (monoclinic and tetragonal) and to detect the presence of bulk WO_3 crystallites. The ZrO_2 diffraction features of interest are the (11$\bar{1}$) and (111) reflections of the monoclinic phase and the (111) reflection of the metastable tetragonal phase. Since these reflections overlap even in samples oxidized at high temperatures, they were resolved using a model proposed by Schreiner and Jenkins (29), which fits both the instrumental and the wavelength-breadth components to asymmetric Lorentzians. These pattern-resolved reflections, corrected for $K\alpha_1$–$K\alpha_2$ wavelength breadth and for instrumental broadening, were used to calculate the tetragonal volume percentage (V_t) and the tetragonal and monoclinic crystallite sizes in these crystallographic directions.

The integrated areas under the resolved reflections (I_t, I_m) were used to calculate the intensity ratio (X_t) (Eq. [1]) and then V_t using an empirical nonlinear relationship (Eq. [2]) obtained by Toraya *et al.* (30) from physical mixtures of monoclinic and tetragonal ZrO_2. The Scherrer relationship (Eq. [3]) (31) was used to calculate crystallite sizes (D_{hkl}) using the integral line widths (B_{hkl}) of the monoclinic and tetragonal pattern-resolved reflections and a shape factor equal to one:

$$X_t = \frac{I_t(111)}{I_m(11\bar{1}) + I_m(111) + I_t(111)} \quad [1]$$

$$V_t = \frac{1.311(1 - X_t)}{1.311 - 0.311X_t} \quad [2]$$

$$D_{hkl} = \frac{S\lambda}{B_{hkl}\cos\theta}. \quad [3]$$

Thermal Analysis

Weight changes during sample oxidation (0.030–0.100 g) were measured by thermal gravimetry (Mettler TA-2000C). Weight changes were measured at a heating rate of 0.167 K s^{-1} in a 20% O_2/He stream. Heat changes as a result of crystallization of amorphous zirconia were measured with a differential scanning calorimeter (Dupont 2100, 0.167 K s^{-1}), using samples (0.025–0.030 g) sealed in aluminum containers and γ-Al_2O_3 samples as reference.

Temperature-programmed reduction studies were carried out in a Quantasorb surface area analyzer (Quantachrome Corporation) modified with electronic mass flow meters, a programmable furnace, and on-line 13X molecular sieve traps in order to remove the water formed during reduction. A 20% H_2/Ar mixture (Matheson UHP, certified mixture) flowing at 1.33 $cm^3\,s^{-1}$ was used to reduce samples (0.025–0.200 g) held within a 4-mm-I.D. quartz u-tube cell containing a quartz thermowell directly in contact with the sample bed. Reduction rates were obtained by thermal conductivity measurements of the H_2 concentration in the exit stream as the sample temperature was raised from room temperature to 1400 K at 0.167 K s^{-1} and held for 0.5 h. The output analog signal was calibrated using the complete reduction of a standard CuO powder (Aldrich, 99.995%) in order to determine H_2 consumption rates.

X-Ray Absorption Spectroscopy

X-ray absorption spectra were obtained using beamlines 4-1 and 4-3 at the Stanford Synchrotron Radiation Laboratory (SSRL). Spectra were measured in transmission mode, with Ar in the ion chamber detectors. Monochromators on both beamlines were equipped with Si(220) crystals, detuned to 50% of the maximum inlet signal intensity in order to minimize harmonics. Data points were obtained at 0.25 eV increments near the W-L_1 and W-L_{III} edges (12100 and 10207 eV) and at 0.04 $Å^{-1}$ increments in the extended fine structure (EXAFS) region. A Hf impurity (~0.5 wt.%) in ZrO_2 limited the EXAFS to the range between the W-L_{III} (10207 eV) and Hf-L_{III} (10739 eV) edges.

All catalyst samples were diluted with SiO_2 to 2.2 wt.% W, pressed into wafers, crushed, and sieved to retain particles with 0.18–0.25 mm diameter. Sieved powders were packed into quartz capillaries (0.9 mm diameter with 0.1 mm wall thickness) and supported horizontally in a rectangular X-ray beam path (0.2 mm × 6.0 mm). Four heat cartridges in a copper heat sink supplied heat uniformly to the capillary cell. Samples were dehydrated and oxidized in air flowing through the capillary (0.167 $cm^3\,s^{-1}$, Matheson, Ultra Zero).

In processing the spectra, the background was removed by fitting a straight line to the pre-edge region and a third-order polynomial spline to the EXAFS region. The spectra were normalized to the step height, measured at the edge energy. The edge energy is defined as the energy at the first

inflection point for W-L_{III} spectra and as the first inflection point beyond the pre-edge feature for W-L_I spectra. The normalized EXAFS was converted to units of $Å^{-1}$ and then Fourier transformed over the range 2–11.5 $Å^{-1}$ (32). Small changes in the W-L_I near-edge spectra were quantified by subtracting a bulk WO_3 reference spectrum from the sample spectra, using previously reported procedures (33).

Catalytic Measurements

Kinetic studies were carried out in high-pressure flow and glass recirculating batch reactors described previously (34). Catalyst samples were sieved to retain particles with diameters between 0.25 and 0.50 mm. These samples were placed along with quartz powder of similar particle size into the reactors. Before catalytic tests, samples were pretreated at 773 K in flowing air (8.33 $cm^3\ s^{-1}$, Matheson, Ultra Zero) for 3 h and then reduced at reaction temperature in flowing hydrogen (8.33 $cm^3\ s^{-1}$, Matheson, UHP) for 1 h. Oxygen and water impurities in H_2 were removed using a Pd/Al_2O_3 catalyst (Johnson–Mathey) and a molecular sieve trap held at ambient temperature. Gas chromatography (Hewlett–Packard GC/MS 5890/5993, 50-m Ultra-2 column for C_7 separations and 30-m DB-Wax column for xylene separations) with flame ionization and mass spectrometric detection was used to measure product distributions. Reaction rates are reported as W atom turnovers, defined as the moles of reactant converted per W atom per second. Product selectivities are reported on a carbon basis as the percentage of the converted reactant that appears as a given product.

n-Heptane isomerization kinetic experiments were carried out between 453 and 513 K at total pressures between 300 and 2500 kPa in a plug-flow reactor. Electronic mass flow controllers were used to control gas flow rates and a liquid syringe pump was used to introduce *n*-heptane (Fluka, >99.7%) into a heated mixing zone at 523 K before entering the reactor.

o-Xylene isomerization kinetic experiments were carried out in a glass recirculating batch reactor at 523 K and a total pressure of 107 kPa (0.67 kPa *o*-xylene, 106 kPa H_2 or He, 0.030 g sample). This reactor has a total volume of 693 cm^3, a gas recirculation rate of 4.17 $cm^3\ s^{-1}$, and it is operated at less than 2% reactant conversion per pass in order to ensure gradientless operation (34). The reactor is evacuated using mechanical and diffusion pumps isolated from the system by liquid nitrogen traps. *o*-Xylene (NBS, >99.995%), degassed using several freeze–evacuation–thaw cycles, was admitted as a vapor from liquid held at room temperature.

Hydrogen transfer pathways were studied by H–D isotopic exchange reactions in the glass recirculating batch reactor. Deuterium/*n*-heptane (343 K, 97 kPa D_2, 3.7 kPa *n*-heptane) and deuterium/*o*-xylene (523 K, 106 kPa D_2, 0.67 kPa *o*-xylene) exchange rates were measured during isomerization reactions. The deuterium content in reactants and products was calculated from mass spectrometric data using matrix techniques that account for natural ^{13}C abundance and ion fragmentation kinetics (35).

RESULTS AND DISCUSSION

ZrO_2 Crystal Structure and Crystallite Size

Amorphous $ZrO_x(OH)_{4-2x}$ powders treated in air above 723 K convert to crystalline ZrO_2 with tetragonal, monoclinic, or cubic structures. At temperatures below 1443 K, monoclinic ZrO_2 is the thermodynamically stable crystal structure for crystallites larger than 10 nm (36). Metastable tetragonal ZrO_2 crystallites smaller than 10 nm often form after oxidation at temperatures slightly above the ZrO_2 crystallization temperature (723 K). The fraction of tetragonal ZrO_2 crystallites formed is strongly influenced by the nature of the $ZrO_x(OH)_{4-2x}$ precursors and by the methods used in their synthesis (37). After oxidation at higher temperatures (>900 K), ZrO_2 crystallites sinter and become predominately monoclinic, regardless of precursor or synthetic method. Pure tetragonal ZrO_2 crystallites, however, may be stabilized by impregnation with metal oxides before high-temperature oxidative treatments (38).

WO_x species strongly influence $ZrO_x(OH)_{4-2x}$ crystallization into ZrO_2. Impregnation of $ZrO_x(OH)_{4-2x}$ with ammonium metatungstate solutions stabilizes tetragonal ZrO_2 crystallites after high-temperature oxidative treatments (90% tetragonal for 7.9 wt.% W/ZrO_2 vs 3% tetragonal for pure ZrO_2 at 1073 K). This stabilization of tetragonal ZrO_2 crystallites is shown in Fig. 1a, which compares the tetragonal ZrO_2 content in samples containing 7.9 wt.% W with pure ZrO_2 samples at various oxidation temperatures. In addition to stabilizing tetragonal ZrO_2 crystallites, WO_x surface species inhibit ZrO_2 crystallite sintering, leading to smaller crystallites than in pure ZrO_2 (Fig. 1b). In pure ZrO_2, the tetragonal content decreases markedly after oxidation above 800 K. When WO_x surface species are present (7.9 wt.% W), this phase transition occurs at higher oxidation temperatures (>1073 K). This phase transition is not accompanied by a rapid increase in crystallite size; the sizes of tetragonal and monoclinic crystallites are similar and much smaller than those in pure ZrO_2. This suggests that WO_x species strongly interacting with ZrO_2 crystallites inhibit sintering even at high oxidation temperatures. It appears that a critical crystallite size is reached (∼20 nm), above which tetragonal crystallites become unstable and transform into monoclinic crystallites of identical size.

The tetragonal content in ZrO_2 also depends on WO_x concentration at each oxidation temperature. For example, after oxidative treatments at 1073 K, the tetragonal ZrO_2 percentage increases and the crystallite size decreases with increasing WO_x concentration (Fig. 2). A minimum ZrO_2 crystallite size (16 nm) is reached by samples containing 7.9 wt.% W, and crystallites retain this size as WO_x concentration increases further. At WO_x concentrations above

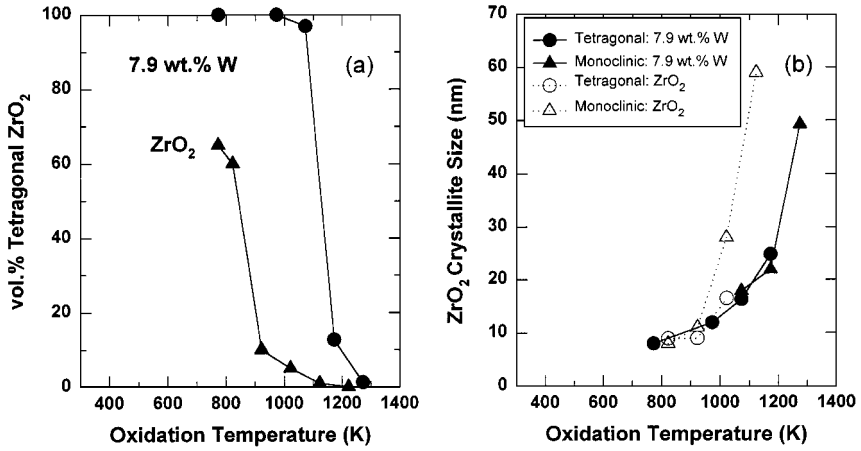

FIG. 1. Powder X-ray diffraction results of ZrO_2 and WO_x–ZrO_2 (7.9 wt.% W) samples showing stabilization of (a) the tetragonal ZrO_2 phase and (b) the ZrO_2 crystallite size with WO_x surface species at various oxidation temperatures.

12 wt.% W, ZrO_2 crystallites are purely tetragonal and monoclinic WO_3 crystallites become detectable by X-ray diffraction. Samples with bulk WO_3 crystallites can also be identified visually by their light yellow color, instead of the white color of the rest of the samples.

Catalyst Surface Area Measurements

$ZrO_x(OH)_{4-2x}$ powders have a high surface area (289 $m^2\ g^{-1}$) after drying at 383 K for 12 h. This surface area decreases markedly after oxidative treatments above the ZrO_2 crystallization temperature (723 K) (Fig. 3). The sintering of ZrO_2 crystallites is inhibited by impregnating metatungstate ions onto $ZrO_x(OH)_{4-2x}$ before oxidation. The surface area of the 7.9 wt.% W sample is about 40 $m^2\ g^{-1}$ greater than that in ZrO_2 samples after oxidation between 773 and 1173 K (Fig. 3). For example, after oxidation at 1073 K, the surface area of pure ZrO_2 is 6 $m^2\ g^{-1}$, while the surface area of a sample containing 7.9 wt.% W is 51 $m^2\ g^{-1}$. Surface areas for all samples become quite similar after oxidation above 1173 K, apparently because WO_x species are ineffective at stabilizing the ZrO_2 surface at these temperatures.

WO_x species are not the only reported textural promoters of ZrO_2. Several other oxides also inhibit ZrO_2 crystallite sintering at high oxidation temperatures (38). Strongly bound surface oxides inhibit intercrystallite sintering by reducing the rate of ZrO_2 surface diffusion (39). These surface oxides may lose their effectiveness at high temperatures because they diffuse into the bulk, decompose and desorb, or "dewet" and agglomerate to form poorly interacting clusters as a separate phase. At high oxidation temperatures (>1173 K), surface WO_x species agglomerate into monoclinic WO_3 crystallites and become less effective sintering inhibitors. SO_x species also inhibit the loss of ZrO_2 surface area after oxidative treatments (3). However, these species decompose and desorb as SO_3 at relatively low oxidation

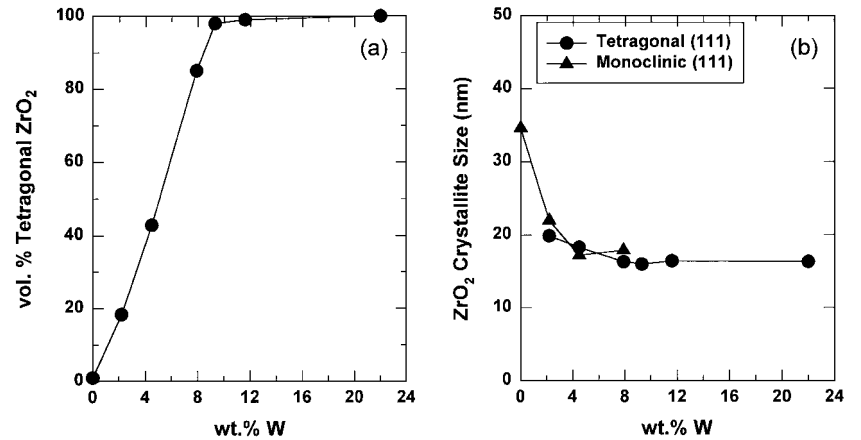

FIG. 2. Powder X-ray diffraction results of WO_x–ZrO_2 samples showing stabilization of (a) the tetragonal ZrO_2 phase and (b) the ZrO_2 crystallite size with various WO_x concentrations after oxidation at 1073 K.

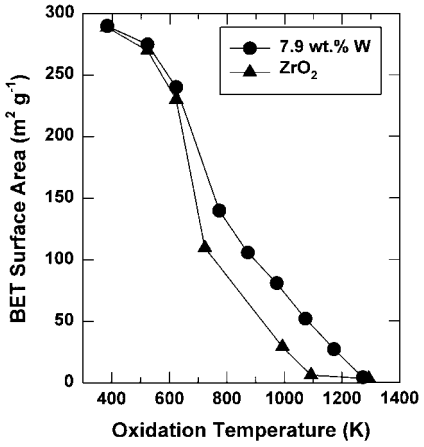

FIG. 3. N_2 physisorption BET surface area data of ZrO_2 and WO_x–ZrO_2 (7.9 wt.% W) samples at various oxidation temperatures.

temperatures (~873 K), leading to rapid ZrO_2 sintering above 873 K (40).

The surface area of WO_x–ZrO_2 samples also depends on WO_x coverage. At a given oxidation temperature, surface area increases with WO_x concentration (Fig. 4). An asymptotic value of surface area is reached near 7.9 wt.% W after oxidation at 873 or 1073 K. The nominal WO_x surface densities on 7.9 wt.% W samples oxidized at 873 and 1073 K are 2.3 and 5.0 W nm^{-2}, respectively. These WO_x surface densities are below the theoretical monolayer capacity (7.3 W atoms nm^{-2} (41)), yet further increases in WO_x concentration do not lead to higher surface areas. The WO_x concentration required for maximum surface area (7.9 wt.% W) is independent of oxidation temperature and corresponds to submonolayer coverages. In addition, the maximum tetragonal content was also detected at this WO_x concentration. These data suggest that a fixed number of strong binding sites for metatungstate ions exist on $ZrO_x(OH)_{4-2x}$ powders (0.8 W nm^{-2}) and impregnation with excess metatungstate ions (>7.9 wt.% W) leads to WO_x species that are not effective at additional stabilization of ZrO_2 crystallites. Thus, it appears that these weakly bound WO_x species may form WO_x clusters below WO_x surface densities corresponding to the theoretical monolayer. This idea of a maximum number of strong binding sites is supported by the results of Fuentes (42), who found that WO_x–ZrO_2 samples prepared by coprecipitation of $ZrO_x(OH)_{4-2x}$ and excess ammonium metatungstate attain maximum W concentration of 8 wt.% W, after washing with a NH_4OH solution of pH 10, a process that removes the weakly bound WO_x species.

ZrO_2 crystallite phase and size can be controlled by adjusting oxidation temperature and WO_x loading. These experimental variables are useful in the design of catalysts with a given WO_x surface density but higher surface areas. For example, a sample with 21 wt.% W oxidized at 823 K (140 m^2 g^{-1}) has the same nominal WO_x surface density (5.0 W nm^{-2}) as a 7.9 wt.% W sample oxidized at 1073 K (50 m^2 g^{-1}). We have also detected by X-ray diffraction the incipient formation of WO_3 crystallites at about 9 W nm^{-2}, irrespective of surface area, WO_x concentration, or oxidation temperature. The important effects of WO_x surface density on catalytic activity and W^{6+} reducibility are discussed below.

Thermal Analysis

Weight changes during thermal decomposition of $ZrO_x(OH)_{4-2x}$ and WO_x–ZrO_2 (7.9 wt.% W) samples are shown in Fig. 5. The $ZrO_x(OH)_{4-2x}$ sample loses 19% of its weight during decomposition to ZrO_2 and heating to 1073 K. This weight loss and the weight loss during ammonium metatungstate decomposition ($(NH_4)_6H_2W_{12}O_{40} \rightarrow WO_3$; 6.5 wt.%) were used to calculate nominal WO_x concentrations (wt.% W) for WO_x–ZrO_2 samples after

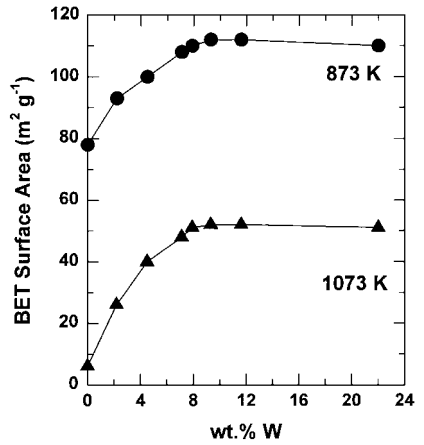

FIG. 4. N_2 physisorption BET surface area data of WO_x–ZrO_2 samples at various WO_x concentrations after oxidation at 873 and 1073 K.

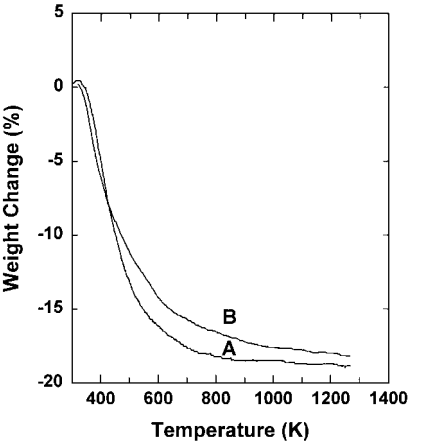

FIG. 5. Thermogravimetric weight loss data of (A) $ZrO_x(OH)_{4-2x}$ and (B) WO_x–$ZrO_x(OH)_{4-2x}$ (7.9 wt.% W) samples heated at 0.167 K s^{-1} in air.

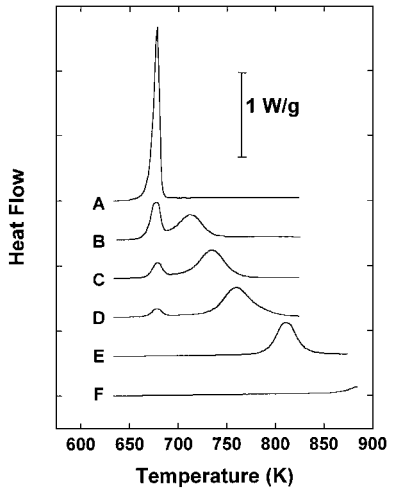

FIG. 6. Differential scanning calorimetry data showing the influence of WO_x concentration on ZrO_2 crystallization exotherms for (A) $ZrO_x(OH)_{4-2x}$ and WO_x–$ZrO_x(OH)_{4-2x}$ samples with (B) 2.2 wt.% W, (C) 4.5 wt.% W, (D) 7.9 wt.% W, (E) 16 wt.% W, and (F) 21 wt.% W heated at 0.167 K s^{-1} in air.

oxidation. Elemental analysis (Galbraith Laboratories, Inc., Knoxville, TN) of a WO_x–ZrO_2 sample oxidized at 1073 K verified the accuracy of this method (11.9 wt.% W nominal vs 11.6 wt.% W analyzed) and confirmed that WO_x species were not lost by sublimation during high-temperature oxidative treatments.

Differential scanning calorimetry (DSC) data (Fig. 6) contain a single sharp exotherm at 679 K for a pure $ZrO_x(OH)_{4-2x}$ sample as a result of ZrO_2 crystallization. $ZrO_x(OH)_{4-2x}$ samples impregnated with ammonium metatungstate solutions have an additional broader exotherm that increases in relative area and occurs at increasing temperatures with increasing WO_x concentration. The integrated area of these two exotherms remains constant when normalized by the weight of ZrO_2 in these samples ($\sim$120 J g-ZrO_2^{-1}), which indicates that both of these exotherms are due to ZrO_2 crystallization. The relative area of the first exotherm is a measure of the fraction of $ZrO_x(OH)_{4-2x}$ crystallites that contain no WO_x surface species. It is evident that this area is small even for the WO_x–$ZrO_x(OH)_{4-2x}$ sample with the lowest WO_x concentration (2.2 wt.% W, Fig. 6B), indicating that incipient wetness impregnation leads to WO_x species that are very well dispersed.

The relative area of the second exotherm increases and occurs at higher temperatures with increasing WO_x concentration. WO_x species on the surface of amorphous zirconia crystallites delay the onset of crystallization by binding to nucleation sites and by limiting the rate of ZrO_x surface diffusion, both of which are required for crystallization (43). As a result, the crystallization temperature of ZrO_2 increases with increasing WO_x concentration because more nucleation sites become blocked and higher ZrO_x surface diffusion rates are required to reach exposed nucleation sites. This inhibition of ZrO_x surface diffusion by WO_x species also prevents the rapid sintering of ZrO_2 crystallites and loss of surface area as reported above.

Thermal analysis results for the WO_x–$ZrO_x(OH)_{4-2x}$ samples heated to higher temperature (1273 K) have no additional features that could arise from decomposition or loss of WO_x species. This thermal stability of WO_x species differs markedly from the poor stability of SO_x species supported on ZrO_2. Thermal analysis has detected SO_x decomposition ($\sim$873 K) to volatile SO_2 and SO_3 products in air, H_2S in H_2, and H_2SO_4 when H_2O is present (40). Decomposition to H_2S occurs at even lower temperatures when Pt crystallites are present. These difficulties limit the applicability of SO_x–ZrO_2 catalysts, while the inherent stability of WO_x species permits catalyst regeneration and operation at much higher temperatures.

Temperature-Programmed Reduction

Temperature-programmed reduction (TPR) studies of supported metal oxides have been used extensively to provide semi-quantitative descriptions of domain sizes and monolayer capacities for surface oxides (44). Dispersed metal oxides tend to reduce at higher temperatures than bulk crystallites because of strong M–O bonds with the oxide surface and a lack of metal oxide nearest neighbors to share the reduced charge. TPR methods are often useful indicators of the onset of bulk metal oxide crystallite formation, caused by a progression from isolated species to two-dimensional structures and three-dimensional clusters. These methods have been applied to MoO_3 on many supports (45) and to WO_3 species on Al_2O_3 and SiO_2 (46).

Temperature-programmed reduction profiles are shown in Fig. 7 for bulk WO_3, WO_x–Al_2O_3, $H_3PW_{12}O_{40}$ on SiO_2, and for a range of WO_x concentrations on ZrO_2. All samples

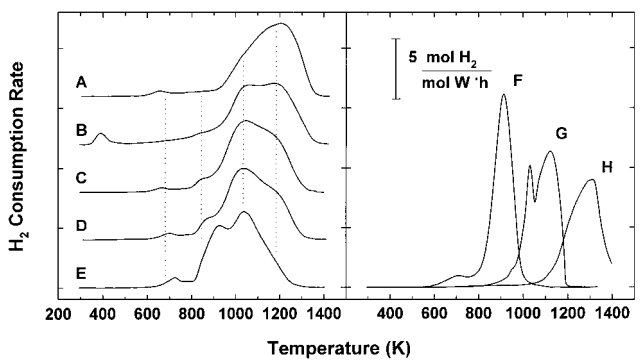

FIG. 7. Temperature-programmed reduction profiles of WO_x–ZrO_2 samples (0.025–0.200 g) after oxidation at 1073 K: (A) 2.2 wt.% W, (B) 0.3% Pt–7.9 wt.% W, (C) 9.5 wt.% W, (D) 11.6 wt.% W, and (E) 21 wt.% W and W standards, (F) 12-tungstophosphoric acid on SiO_2 (30 wt.% W), (G) bulk WO_3, and (H) 7.9 wt.% W/Al_2O_3 heated at 0.167 K s^{-1} (1.33 cm^3 s^{-1}, 20% H_2 in Ar).

reduced to W metal at temperatures below 1323 K, except WO_x–Al_2O_3. Pure ZrO_2 samples showed no significant H_2 consumption up to 1323 K. Three overlapping peaks were detected for the reduction of bulk WO_3 samples (Fig. 7G), which occurs via stepwise reduction: $WO_3 \rightarrow WO_{2.9} \rightarrow WO_2 \rightarrow W$ (46).

The reduction profiles for WO_x–ZrO_2 samples are very broad (800 K) and have four overlapping peaks (Figs. 7A–7E) that occur at similar temperatures at all WO_x concentrations. The first three peaks correspond to the same three reduction steps found in bulk WO_3. A direct comparison with bulk WO_3, however, is impaired by marked differences in crystallite size between bulk and supported samples. An additional reduction step occurs at high temperature (1200 K) in WO_x–ZrO_2 samples; it corresponds to the reduction of WO_x species strongly bound to the ZrO_2 support ($WO_{2.9} \rightarrow W$). These WO_x species reduce at higher temperatures because they contain unreactive oxygen linkages to the ZrO_2 support. As WO_x concentration increases, the relative area of this high-temperature reduction peak decreases, which is consistent with a decreasing fraction of strong W–O–Zr bonds and increasing fraction of WO_x species in domains that reduce at lower temperatures.

The second reduction step ($WO_{2.9} \rightarrow WO_2$) is sensitive to the size of the WO_x domains. At low WO_x concentrations, a large fraction of the WO_x domains bypass this second reduction step and instead reduce directly to W metal ($WO_{2.9} \rightarrow W$) in the third reduction step; apparently there are not enough WO_x neighbors in these small domains to form the stable intermediate WO_2 species. The relative area of this second reduction step increases with increasing WO_x concentration and ultimately approaches that for stoichiometric reduction to WO_2 as in WO_x–ZrO_2 samples containing primarily bulk WO_3 crystallites (21 wt.% W, 1073 K oxidation). Thus, the increase in the area of this second reduction step suggests a growth of WO_3-like domains with W–O–W linkages as WO_x concentration increases; these domains reduce at lower temperatures than isolated WO_x species.

WO_x species on ZrO_2 reduce at significantly lower temperatures than WO_x on Al_2O_3 at similar surface densities. For example, reduction of the 2.2 wt.% W on ZrO_2 (2.7 W nm^{-2}) sample is complete by 1350 K, whereas reduction of the 6 wt.% W on Al_2O_3 (2.4 W nm^{-2}) sample is not finished at 1400 K. At low WO_x surface densities, the reduction temperature of these dispersed WO_x species is determined by the strength of the W–O bonds that contain oxygens shared with the support. The higher reduction temperature of the WO_x–Al_2O_3 sample suggests that the W–O–Al bonds are stronger than the W–O–Zr bonds. At higher WO_x surface densities, the WO_x polyhedra are connected by W–O–W bonds, and the first two reduction steps of these polytungstate domains on ZrO_2 occur at temperatures similar to those required for the reduction of WO_x domains in heteropolyacids ($H_3PW_{12}O_{40}$). This suggests that the onset of reduction of polytungstate domains is not influenced by the support when there are enough WO_x neighbors to share the reduced charge and bridging W–O–W bonds that can be broken.

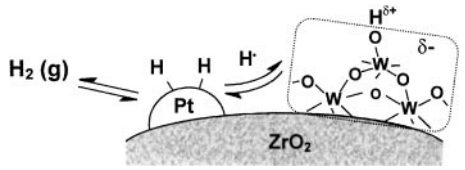

SCHEME 1. Generation of Brønsted acid sites in hydrogen by slight reduction and delocalization of negative charge in WO_x domains.

The addition of Pt (0.3 wt.%) to WO_x–ZrO_2 (12.7 wt.% W) strongly affects the first reduction step ($WO_3 \rightarrow WO_{2.9}$), which shifts from 700 to 350 K (Fig. 7B). This suggests that slight reduction can occur during H_2 pretreatment and during *n*-alkane reactions at 440–500 K. The ability of WO_x domains to undergo slight reduction by delocalizing the net negative charge may be linked with the strong acidity appearing on WO_x domains on ZrO_2, for which the domain sizes become large enough to delocalize the electron charge over several W atoms. These reducible WO_x domains may act as redox sites required for the formation of H^+ species from H_2 and alkanes on WO_x-based solid acids (Scheme 1). The accommodation of a proton by electron transfer and charge delocalization across an extended W–O network results in electronic structures similar to those of heteropolyacids (47). This simple mechanism may also account for the ability of H atoms to desorb carbocations as neutral hydrocarbons and to regenerate neutral WO_3 domains (Scheme 2) and for the observed effects of hydrogen on the rate and selectivity of *n*-heptane and *o*-xylene isomerization reactions.

X-Ray Absorption Spectroscopy

W-L_I near-edge spectra for Na_2WO_4 and $(NH_4)_6H_2W_{12}O_{40}$ standards and for a WO_x–ZrO_2 sample (11.7 wt.% W) before and after high-temperature oxidation (1073 K) are shown in Fig. 8. The pre-edge feature at −10 eV reflects a $2s \rightarrow 5d$ electronic transition that is dipole-forbidden in centrosymmetric structures, but becomes allowed in

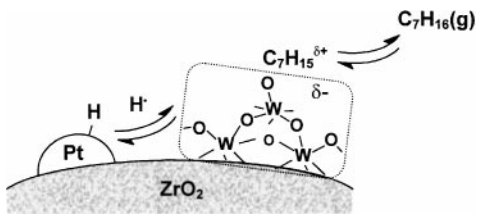

SCHEME 2. Stabilization of carbocations by slight reduction of WO_x domains.

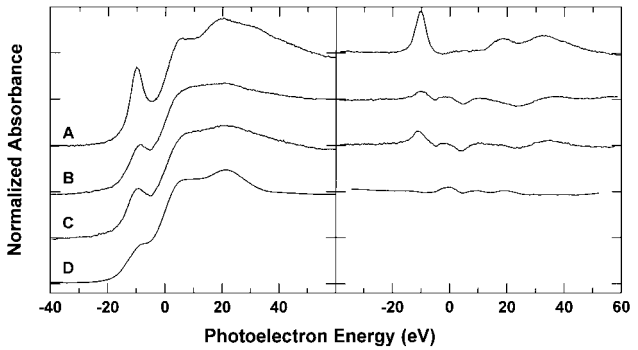

FIG. 8. Normalized W-L_I near-edge spectra of WO_x standards and WO_x–ZrO_2 samples: (A) dehydrated Na_2WO_4, (B) 11.6 wt.% W after 1073 K, (C) 11.6 wt.% W after 423 K, and (D) $(NH_4)_6H_2W_{12}O_{40}$. Difference spectra at right, with equivalent vertical scale, calculated by subtracting the WO_3 spectrum from the sample spectrum. Spectra recorded *in situ* at 298 K after dehydration at 423 K.

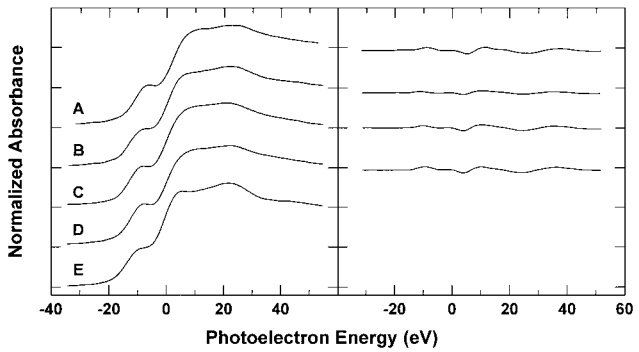

FIG. 9. Normalized W-L_I near-edge spectra of WO_x–ZrO_2 samples (1073 K oxidation): (A) 2.2 wt.% W, (B) 11.6 wt.% W, (C) 0.3 wt.% Pt–12.7 wt.% W, (D) 21 wt.% W, and (E) bulk WO_3. Difference spectra at right, with equivalent vertical scale, calculated by subtracting the WO_3 spectrum from the sample spectra. Spectra recorded *in situ* at 298 K after dehydration at 723 K.

tetrahedral or distorted octahedral structures because of *p–d* orbital mixing (48). Thus, changes in the intensity of this pre-edge feature reflect changes in the symmetry of the W absorber (49). This feature has been used to determine the distribution of W among octahedral and tetrahedral structures in Al_2O_3- and TiO_2-supported WO_x catalysts (50, 51). These studies have concluded that W atoms can be 4-, 5-, or 6-coordinate depending on the W coverage and the state of hydration. The spectrum of a $ZrO_x(OH)_{4-2x}$ sample impregnated with an aqueous ammonium metatungstate solution and dried *in situ* at 423 K (Fig. 8C) differs from the spectrum of pure ammonium metatungstate (Fig. 8D), indicating that a reaction occurs between the aqueous metatungstate ions and the $ZrO_x(OH)_{4-2x}$ surface during impregnation. After oxidation at 1073 K, which sinters the ZrO_2 crystallites and markedly increases the WO_x surface density, the spectrum changes only slightly (Fig. 8B), suggesting that the local structure and symmetry of the WO_x species does not change significantly after oxidative treatments that lead to catalytically active WO_x–ZrO_2 samples.

W-L_I near-edge spectra for bulk WO_3 and WO_x–ZrO_2 samples oxidized at 1073 K with various WO_x concentrations are shown in Fig. 9. All spectra were measured at room temperature after *in situ* dehydration in He at 823 K. The similarity among the three WO_x–ZrO_2 spectra and the spectrum of bulk WO_3 is confirmed by subtraction of the bulk WO_3 spectrum from each of the three WO_x–ZrO_2 spectra (Fig. 9). These difference spectra differ markedly from the difference spectrum of Na_2WO_4 that contains W atoms only in tetrahedral sites (Fig. 8A). The difference spectra show that WO_x structures have a distorted octahedral symmetry that is insensitive to WO_x concentration in a concentration range that strongly influences catalytic behavior.

The W-L_{III} fine structure of the samples in Fig. 9 was used to obtain the radial structure functions shown in Fig. 10. There are only slight differences among the four samples containing different WO_x concentrations and bulk WO_3. W centers in bulk WO_3 crystallites reside in relatively low symmetry positions. For example, in monoclinic WO_3 there are 24 different W–O distances per unit cell, ranging from 1.715 to 2.215 Å (52). Because of this structural disorder, coordination numbers and distances derived from the W radial structure functions are poorly defined. Figure 10 shows, however, that WO_x structures present on the surface of ZrO_2 at all WO_x concentrations have a static disorder similar to that in bulk WO_3. W-L_I near-edge spectra and W-L_{III} radial distribution functions in all WO_x–ZrO_2 samples resemble those of bulk WO_3; therefore, W atoms reside in structures with distorted octahedral symmetry resembling that in bulk WO_3 for all WO_x concentrations and pretreatment conditions. As a result, significant differences in catalytic activity within these samples cannot be simply

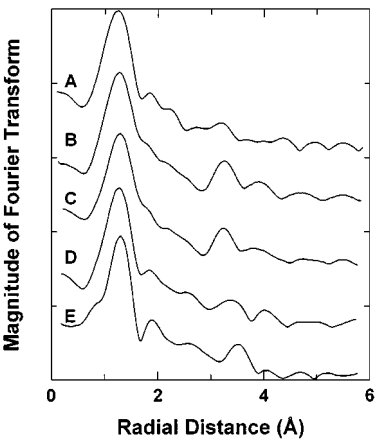

FIG. 10. W-L_{III} radial structure functions, not phase or amplitude corrected, of WO_x–ZrO_2 samples after oxidation at 1073 K: (A) 2.2 wt.% W, (B) 11.6 wt.% W, (C) 0.3 wt.% Pt–12.7 wt.% W, (D) 21 wt.% W, and (E) bulk WO_3. Spectra recorded *in situ* at 298 K after dehydration at 723 K.

explained by differences in the local symmetry of the WO_x octahedra, but may be explained instead by differences in the size of the WO_x extended domain. We discuss how rates of *o*-xylene isomerization relate to the WO_x domain size determined by UV–visible spectroscopy below.

Catalytic Isomerization of n-Heptane

The addition of a metal function (0.3 wt.% Pt) to WO_x–ZrO_2 leads to high *n*-heptane isomerization turnover rates and selectivities at low temperatures (18). The isomerization selectivity at 473 K and 50% *n*-heptane conversion is 85% on Pt/WO_x–ZrO_2. These isomerization selectivities are much higher than on Pt/SO_x–ZrO_2 (<50%) and on other mesoporous acid catalysts. Here, we expand our previously reported results (18) in order to contrast these results with the effects of H_2 on *o*-xylene isomerization catalyzed by WO_x–ZrO_2 samples without a metal function.

On Pt/WO_x–ZrO_2, *n*-heptane isomerization turnover rates depend weakly on H_2 gas phase concentration. Turnover rates on Pt/WO_x–ZrO_2 become negative order in H_2 ($0 \rightarrow -0.5$) as H_2 pressures increase. These data are consistent with quasi-equilibrated hydrogen transfer steps, which lead to short surface lifetimes, low steady-state carbocation coverages, and desorption of carbocations before β-scission occurs. On Pt/WO_x–ZrO_2, *n*-heptane isomerization occurs on a surface sparsely populated with carbocations and surface isomerization steps are rate-determining (Scheme 3). In effect, carbocation formation and desorption by hydrogen transfer are quasi-equilibrated and carbocation coverages are proportional to *n*-heptane pressure, leading to the observed first-order dependence on *n*-heptane concentration. The negative H_2 pressure order arises from competitive binding of H^+ and carbocations at WO_x sites, which causes carbocation surface densities to decrease with increasing H_2 pressure. On Pt/SO_x–ZrO_2, *n*-heptane isomerization turnover rates have a positive H_2 order (0.9) and they increase when hydrogen transfer cocatalysts, such as adamantane, are added to *n*-heptane reactants. Slow hydrogen transfer reactions delay carbocation desorption and lead to long carbocation surface residence times and low isomer selectivity (6).

Pt/WO_x–ZrO_2 catalyzes H_2 activation and storage of H atoms and provides rapid carbocation neutralization and desorption pathways, which prevent extensive cracking of adsorbed carbocations. This mechanistic conclusion is confirmed by the rapid isotopic exchange between *n*-C_7H_{16} and D_2 observed on Pt/WO_x–ZrO_2 during *n*-heptane isomerization (18). H–D equilibrium between *n*-C_7H_{16} and D_2 occurs much more rapidly than isomerization on Pt/WO_x–ZrO_2. These data show that *n*-heptane adsorbs, exchanges with a surface hydrogen pool initially consisting of D atoms, and frequently desorbs before isomerization occurs.

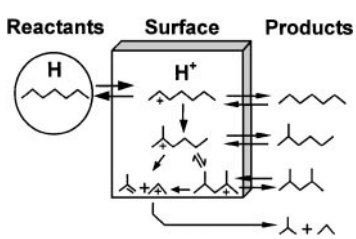

SCHEME 3. *n*-Heptane isomerization on Pt/WO_x–ZrO_2.

TABLE 1

Irreversible Chemisorption Uptake[a] of H_2, O_2, and CO on Pt/WO_x–ZrO_2 (0.3 wt.% Pt, 10 wt.% W)

Reduction temperature (K)	H/Pt	O/Pt	CO/Pt
473	0.63	1.25	0.30
673	0.092	2.04	0.050

[a] Room temperature adsorption; irreversibly chemisorbed species are defined as those that cannot be removed by evacuation at 313 K.

H_2 dissociation is required before it can act as a source of hydrogen atoms. Reduced Pt sites on Pt/WO_x–ZrO_2 dissociate and store H atoms required for hydrogen transfer and carbocation desorption steps. As a result, Pt clusters on Pt/WO_x–ZrO_2 catalysts chemisorb significant amounts of H_2 at room temperature and catalyze exchange of H atoms between D_2 and "unreacted" *n*-heptane.

Pt dispersion measurements after H_2 reduction at 473 K using H_2, O_2, and CO site titrations show that apparent Pt dispersions measured by hydrogen uptake exceed those obtained from CO chemisorption (Table 1), suggesting that hydrogen adatoms spillover onto WO_x centers during H_2 chemisorption at room temperature. O_2 uptakes are much higher than those of H_2 or CO, suggesting that WO_x species reduce slightly during H_2 treatments at typical isomerization reaction temperatures. At higher reduction temperatures, H_2 uptakes decrease and O_2 uptakes increase; these phenomena appear to be related to the decoration of Pt crystallites by reduced WO_x, as also proposed to explain similar effects on TiO_2 supported metal particles (53). Thus, hydrogen atoms formed at H_2 dissociation sites may become involved not only in the desorption of adsorbed intermediates, but also in the generation and maintenance of Brønsted acid sites. The formation of Brønsted acid sites during H_2 treatment has been detected by Ebitani *et al.* (54) using infrared measurements of the density of Lewis and Brønsted acid sites in Pt/SO_x–ZrO_2. In their study, H_2 treatments at temperatures typical of catalytic reactions lead to an increase in the density of Brønsted acid sites and to a decrease in the density of Lewis acid sites, suggesting that Lewis acid sites are converted to Brønsted acid sites by contact with H_2. We suggest that a similar mechanism leads to the formation of Brønsted acid sites on Pt/WO_x–ZrO_2

and WO_x–ZrO_2 samples in the presence of H_2 at reaction temperatures. As a result, attempts to measure the number and nature of the acid sites on these materials must be done under reaction conditions.

Catalytic Isomerization of o-Xylene

Acid-catalyzed skeletal isomerization of *o*-xylene (Eq. [4]) was used to probe the acid properties of WO_x–ZrO_2 samples. Xylene isomerization reactions proceed via intramolecular 1,2 methyl shifts on Brønsted acid sites (55). Bimolecular pathways leading to disproportionation side products (toluene and trimethylbenzenes) can also lead to isomerization of xylenes (56). In the absence of intrapellet diffusional restrictions and bimolecular pathways, the relative selectivity to *m*- and *p*-xylenes extrapolated to zero conversion reflects benzenium ion surface lifetimes. Short surface lifetimes lead to *m*-xylene, a product formed by single methyl shifts; longer surface residence times lead to xylene isomer distributions near thermodynamic equilibrium (57)

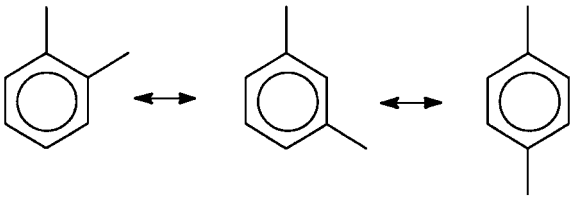

[4]

o-Xylene isomerization was carried out in a recirculating batch reactor at 523 K (0.67 kPa *o*-xylene; 106 kPa H_2). A typical plot of selectivity as a function of *o*-xylene conversion on a 12 wt.% W sample oxidized at 1073 K is shown in Fig. 11. Aromatic hydrogenation, hydrogenolysis, and xylene oligomerization reaction products were not observed

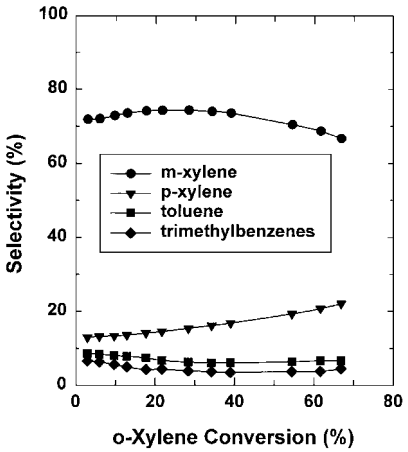

FIG. 11. Selectivity as a function of *o*-xylene conversion on a WO_x–ZrO_2 sample (12 wt.% W) oxidized at 1073 K (reaction conditions: 0.67 kPa *o*-xylene, 106 kPa H_2, 0.0287 g catalyst, 523 K).

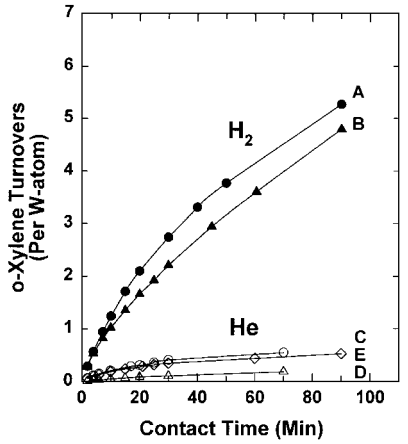

FIG. 12. Influence of hydrogen on *o*-xylene transformations on a WO_x–ZrO_2 (12 wt.% W) sample oxidized at 1073 K (reaction conditions: 0.67 kPa *o*-xylene, 106 kPa H_2 or He, 523 K). Reactor loaded with 0.0287 g for (A) and (B) and run in H_2. Reactor reloaded with 0.0293 g for (C), (D), and (E) and run in He. (B) and (D) were run immediately after (A) and (C) without further pretreatment. (E) was run after oxidative treatment. See Table 2 for pretreatment details.

under these reaction conditions. Tetramethylbenzene, a disproportionation product, became detectable only at high conversions. At low conversions, typical *m*- to *p*-xylene ratios are about 5.6 (thermodynamic equilibrium is 2.3 at 523 K) and disproportionation to isomerization ratios are 0.18. This high *m*-xylene selectivity reflects short benzenium ion lifetimes. *o*-Xylene isomerization turnover rates, based on the total number of W atoms, were used to compare the relative catalytic activity of the WO_x–ZrO_2 samples. Normalization of the isomerization rates by the total number of W atoms is the most conservative estimation of the "true" acid site turnover rate and is a convenient choice in the absence of an accurate measurement of the acid site density in the presence of H_2 under reaction conditions. Initial *o*-xylene isomerization rates are reported at 5–10% conversion in order to avoid including any initial transients.

o-Xylene reactive turnovers (per W atom) are shown as a function of contact time in Fig. 12 for a 12 wt.% W sample oxidized at 1073 K after various H_2 and He pretreatments listed in Table 2. The data in Fig. 12A correspond to the

TABLE 2

Pretreament Conditions and Diluent Gas Composition for *o*-Xylene Isomerization Turnover Data in Fig. 12

Figure 12 data	Diluent	Drying	Reduction
A	H_2	823 K, 2 h	523 K, 2 h
B	H_2	None	None
C	He	823 K, 2 h	523 K, 2 h
D	He	None	None
E	He	823 K, 2 h	523 K, 2 h

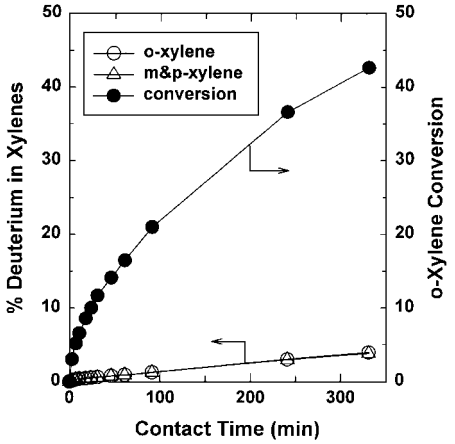

FIG. 13. D_2/*o*-xylene exchange on a WO_x–ZrO_2 (12 wt.% W) sample oxidized at 1073 K (reaction conditions: 0.67 kPa *o*-xylene, 106 kPa D_2, 523 K).

experiment in Fig. 11, which was run in H_2 at 523 K after treatment in dry air for 2 h at 823 K and in H_2 for 2 h at 523 K. Stable isomerization rates were confirmed by flushing the system with H_2 for 1 h at 523 K, refilling the reactor with *o*-xylene/H_2, and remeasuring *o*-xylene isomerization rates (Fig. 12B). Minimal deactivation was detected on this sample after *o*-xylene reactions to near equilibrium conversion for 2 h, as shown by a nearly complete recovery of catalytic activity flushing the system with H_2. The influence of H_2 on *o*-xylene conversions was tested by replacing H_2 with He (Fig. 12C) as an inert diluent. The initial turnover rate was lower in He and rapidly decreased as the sample deactivated. This significant deactivation is shown by the very low rates in Fig. 12D, which was the experiment immediately following flushing the system with He (no oxidation) and refilling with *o*-xylene/He. After these two experiments in He, the sample was reoxidized for 2 h at 823 K and treated in H_2 for 2 h at 523 K and tested again with He as an inert diluent (Fig. 12E). The sample recovered its initial activity, but again deactivated rapidly. The initial activity in He appears to be caused by a sacrificial loss of hydrogen from neighboring adsorbed species, which forms Brønsted acid sites and allows xylene turnovers to occur, but which leaves behind strongly adsorbed unsaturated species. The irreversible buildup of these carbonaceous species leads to the rapid deactivation during *o*-xylene conversions in He. After high-temperature oxidative treatments these samples completely recovered their initial activity.

The mechanism of H_2 promotion in xylene isomerization reactions was probed by replacing H_2 with D_2 and monitoring the rate of exchange between xylenes and D_2 during *o*-xylene isomerization. The deuterium contents (Fig. 13) and the deuterium distributions (Fig. 14) in *o*-xylene, *m*-xylene, and *p*-xylene are identical, indicating that the adsorption of *o*-xylene that leads to an isomerization turnover does not lead to additional deuterium exchange. The rate of deuterium exchange per W atom ($2.3 \times 10^{-4}\,s^{-1}$) is much lower than *o*-xylene isomerization turnover rates ($1.7 \times 10^{-3}\,s^{-1}$). For example, only 1.2% of the H atoms in xylenes have exchanged at 21% *o*-xylene chemical conversion. The deuterium content in the *m*-xylene and *p*-xylene isomers increased with contact time and showed a binomial distribution, suggesting that the surface hydrogen/deuterium species are not in equilibrium with the D_2 in the gas phase. As a result, H atoms formed by H_2 dissociative chemisorption are not frequently involved in the activation or desorption of the xylene reactants. The presence of H_2 is required, however, in order to reverse the occasional desorption of H atoms as H_2, which can occur during *o*-xylene isomerization reactions by the microscopic reverse of the dissociative chemisorption step. These desorption processes lead to the disappearance of Brønsted acid sites and to the formation of strongly adsorbed unsaturated species when xylene isomerization is carried out in the absence of H_2. H_2 can restore these Brønsted acid sites by rereduction of WO_x species or by formation of acidic H_xWO_3 species.

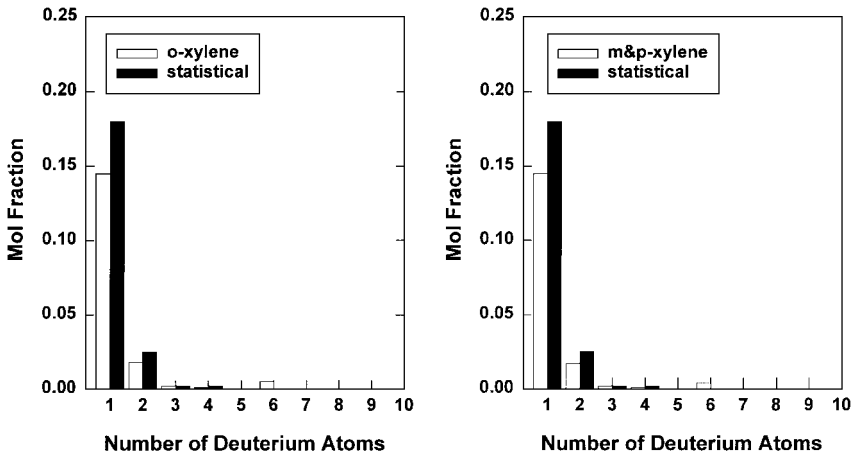

FIG. 14. D distribution in *o*-xylene and in the combination *m*- and *p*-xylenes compared to a statistical distribution of 2.4% D atoms.

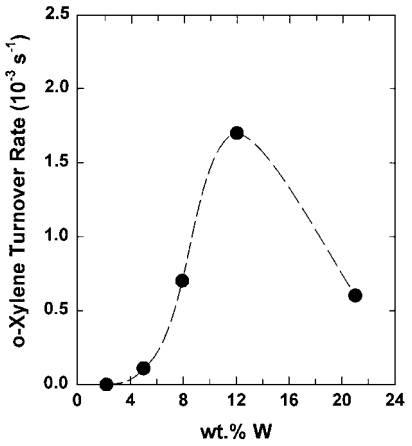

FIG. 15. *o*-Xylene isomerization turnover rates (per W atom) as a function of WO_x concentration on WO_x–ZrO_2 samples oxidized at 1073 K (reaction conditions: 0.67 kPa *o*-xylene, 106 kPa H_2, 523 K).

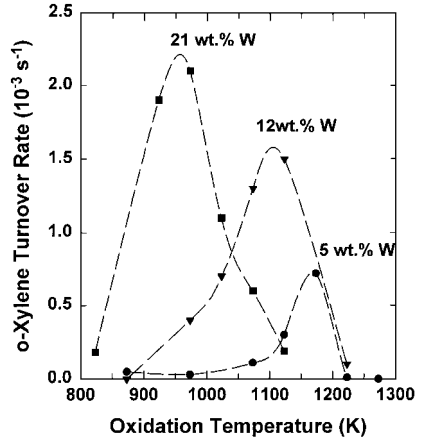

FIG. 16. Influence of oxidation temperature on *o*-xylene isomerization turnover rates on WO_x–ZrO_2 samples at three WO_x concentrations (5, 12, and 21 wt.% W) (reaction conditions: 0.67 kPa *o*-xylene, 106 kPa H_2, 523 K).

o-Xylene isomerization rates on WO_x–ZrO_2 samples with various WO_x concentrations and oxidation temperatures are shown in Figs. 15 and 16. *o*-Xylene isomerization turnover rates for samples oxidized at 1073 K reach a maximum value at a WO_x concentration of 12 wt.% W (Fig. 15), which is similar to that reported by Hino and Arata [12] and later by Santiesteban *et al.* (58) for pentane isomerization reactions. Isomerization rates were negligible on the sample with the lowest WO_x concentration (2.2 wt.% W). The sample with the highest WO_x concentration tested (21 wt.% W) gave low but measurable rates, even though it contains predominately large WO_3 crystallites. Clearly, isomerization rates are not proportional to the number of WO_x sites, but they are strongly affected by the coverage of WO_x on ZrO_2.

WO_x coverage and isomerization rates also depend strongly on oxidation treatment temperatures. ZrO_2 crystallites grow and surface areas decrease with increasing oxidation temperature, which increases the WO_x surface density at a given WO_x concentration. Three freshly prepared WO_x–ZrO_2 samples (5, 12, and 21 wt.% W) that had only been dried at 423 K were oxidized in the quartz reactor at increasing temperatures from 800 to 1300 K. *o*-Xylene isomerization rates were measured on each sample without removing them from the reactor after each oxidation treatment. After catalytic measurements, the reactor was flushed with H_2 at 523 K for 1 h, evacuated, and heated in flowing dry air to the next highest oxidation temperature for 2 h. Isomerization rates (per W atom) on these three samples at several oxidation temperatures are shown in Fig. 16. Each sample reaches maximum isomerization turnover rates at intermediate oxidation treatment temperatures. The sample with the highest WO_x concentration (21 wt.% W) reaches its maximum isomerization rate ($2.1 \times 10^{-3}\,s^{-1}$) after oxidation at 973 K. Samples with lower W content reach maximum rates only after oxidation at higher temperatures (1100–1200 K). Thus, increasing WO_x concentrations in WO_x–ZrO_2 samples decreases the oxidation temperature required to reach maximum catalytic activity and leads to samples with higher surface areas. It appears that a critical WO_x surface density is required in order to obtain a maximum number of acid sites for *o*-xylene isomerization.

Surface areas were measured for these samples at each oxidation temperature and used to convert WO_x concentrations to nominal WO_x surface densities (W nm^{-2}). When isomerization rates for all samples from Fig. 16 are replotted (Fig. 17) as a function of this WO_x surface density, they merge into a single curve with a very sharp maximum rate at about 10 W nm^{-2}. It is apparent that the acid site density depends only on WO_x surface density and that it is independent of the oxidation temperature and WO_x concentration

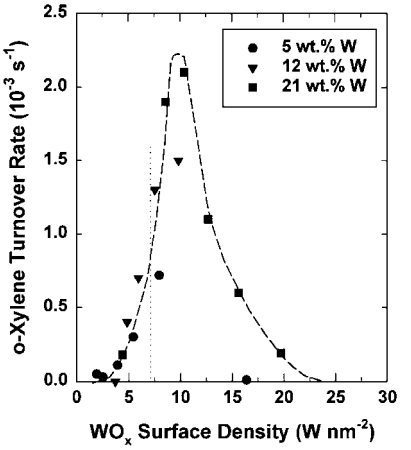

FIG. 17. *o*-Xylene turnover rates replotted from Fig. 16 as a function of nominal WO_x surface density on three WO_x–ZrO_2 (5, 12, and 21 wt.% W) samples oxidized at various temperatures (800–1300 K). The theoretical monolayer capacity for ZrO_2 (7 W nm^{-2}) is marked.

used to obtain a particular WO_x surface density. As a result, a WO_x–ZrO_2 sample with the highest isomerization rate per catalyst weight (1.8×10^{19} s^{-1} g^{-1}) was found on a sample with the highest WO_x concentration (30 wt.% W, 898 K oxidation, 104 m^2 g^{-1}) and was limited only by the solubility of ammonium metatungstate in water.

The critical WO_x surface density at which maximum activity is obtained is higher than the theoretical monolayer capacity of ZrO_2 (7 W nm^{-2}), calculated by assuming corner sharing WO_x octahedra with bond distances derived from monoclinic WO_3; therefore, the most active WO_x–ZrO_2 samples must contain a fraction of the WO_x species in extended three-dimensional networks. At high WO_x surface densities (>10 W nm^{-2}), bulk WO_3 has been detected by X-ray diffraction and therefore isomerization turnover rates normalized to the total number of W atoms must decrease because a large fraction of W atoms reside inside the bulk of these crystallites and become inaccessible to hydrocarbon reactants. At low WO_x surface densities (<5 W nm^{-2}), all the WO_x groups are accessible, and X-ray absorption results indicate that the W atoms reside in a distorted octahedral symmetry similar to that of the most active species. Isomerization rates are, however, very low, suggesting that it is the growth of polytungstate species at WO_x surface densities higher than a monolayer that is required for the formation of acid sites. This narrow range of WO_x surface densities for which WO_x–ZrO_2 samples become catalytically active suggests that high isomerization turnover rates require the presence of WO_x domains of intermediate size, which form selectively as WO_x surface densities reach intermediate values.

Previous analysis of optical absorption edge energies from UV–vis diffuse reflectance spectra for WO_x–ZrO_2 samples with WO_x surface density below 10 W nm^{-2} showed that the number of WO_x nearest neighbors and the WO_x domain size increase with increasing WO_x surface density (18). Optical absorption edge energies were determined by plotting $(\alpha h\nu)^2$ vs $h\nu$ (α, absorbance; hν, photon energy), which assumes that the fundamental optical absorption is the result of a direct electronic transition. The fundamental optical absorption energy for bulk WO_3 crystallites and amorphous WO_x species, however, has been shown to be better approximated by plotting $(\alpha h\nu)^{1/2}$ vs $h\nu$, which results in the indirect absorption edge energy (59). Reanalysis of the absorption spectra based on the indirect transition formalism gives lower edge energies, but the trends remain unchanged (Fig. 18). The position of the UV–visible absorption edge is sensitive to the domain size of transition metal oxides, which is related to the number of nearest metal oxide neighbors sharing a common oxygen (M–O–M bonds) (60). An increase in the domain size results in a decrease in the absorption edge energy. The decrease of the absorption edge with increasing WO_x surface density between 4 and 10 W nm^{-2} reflects an increase in the WO_x domain size. It is

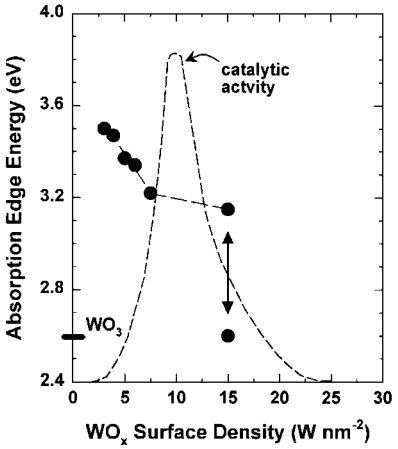

FIG. 18. WO_x domains with intermediate size lead to maximum *o*-xylene isomerization turnover rates. WO_x indirect absorption edge energies determined from absorption data for WO_x–ZrO_2 samples in (18) are plotted over the *o*-xylene isomerization rate curve from Fig. 17. The indirect absorption edge of monoclinic WO_3 is marked for reference.

evident when the *o*-xylene isomerization rate curve is plotted over the UV–visible absorption edge energies (Fig. 18) that increasing WO_x domain sizes lead to increasing isomerization rates at low surface densities (4–10 W nm^{-2}). At higher surface densities (>10 W nm^{-2}), bulk WO_3 was detected by a second electronic transition edge and isomerization rates per W atom decrease as a result of a decrease in WO_x dispersion.

The unique acid properties of WO_x domains of intermediate size appear to be related to their ability to form $W^{6-n}O_x$–(n-H^+) Brønsted acid centers under reducing conditions at low temperatures (Scheme 1 without Pt). Isolated WO_x species that exist at low WO_x surface densities (<5 W nm^{-2}) cannot delocalize the negative charge required for the formation of Brønsted acid centers, whereas polytungstate species that form at intermediate WO_x surface densities reside in an extended network of WO_x species over which an excess negative charge may be delocalized. The ability of these WO_x species to temporarily reduce and reversibly adsorb hydrogen was measured by hydrogen chemisorption uptakes at 523 K. The reversible H_2 uptakes are plotted on the *o*-xylene isomerization rate curve (Fig. 19) and show that reversible H_2 adsorption occurs at reaction temperatures. Maximum hydrogen uptakes were recorded on WO_x–ZrO_2 samples that show maximum catalytic activity, suggesting that the formation of these $W^{6-n}O_x$–(n-H^+) reduced centers is related to the stabilization of carbocationic reaction intermediates. WO_x species present at low surface densities are difficult to reduce and as a result are not able to form these Brønsted acid centers required for xylene reactions. Extended WO_x domains that form at higher WO_x surface densities can delocalize the negative charge required in order to stabilize positively

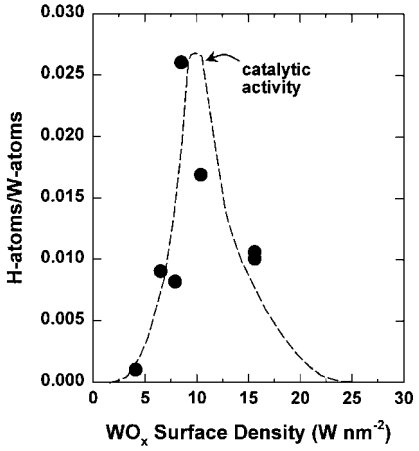

FIG. 19. Reversible H_2 uptakes at 523 K and 45 kPa H_2 on WO_x–ZrO_2 samples oxidized at 1073 K, reduced in H_2 at 523 K for 1 h, and evacuated at 523 K, plotted over *o*-xylene isomerization rates from Fig. 17.

charged species. This delocalization of charge among several WO_x groups to form $W^{6-n}O_x$–(*n*-H^+) acid centers is similar to that previously suggested for the generation of the strong acid sites in heteropolytungstate clusters (47). In 12-tungstophosphoric acid, the neutral $(WO_3)_{12}$ shell around the central PO_4^{3-} anion delocalizes the negative charge over the surface of the shell, which is balanced by three acid hydrogens with a net positive charge to maintain electroneutrality of the cluster.

o-Xylene isomerization turnover rates are strongly influenced by WO_x surface density. Two independent parameters, WO_x concentration and oxidation temperature, are available in order to control the WO_x surface density. Even though turnover rates depend on WO_x surface density, they are not influenced by the specific oxidation temperature or WO_x concentration required in order to obtain a given WO_x surface density. Maximum turnover rates were obtained on WO_x domains of intermediate size (10 W nm^{-2}). These WO_x domains of intermediate size may provide a compromise between the reducibility and the accessibility of WO_x species in supported domains. H_2 is required during *o*-xylene isomerization reactions on WO_x–ZrO_2 for the generation and maintenance of $W^{6-n}O_x$–(*n*-H^+) Brønsted acid centers. For this reason, measurements of the Brønsted acid site density must be carried out under reaction conditions in order to accurately determine the site density present during reaction and to calculate true isomerization turnover rates.

CONCLUSIONS

WO_x–ZrO_2 catalysts active for isomerization reactions at low temperature were prepared by impregnation of $ZrO_x(OH)_{4-2x}$ with a solution of ammonium metatungstate followed by oxidation treatments that sinter the ZrO_2 crystallites and increase the WO_x surface density. Surface area and X-ray diffraction measurements show that dispersed WO_x species inhibit ZrO_2 crystallite sintering and stabilize tetragonal ZrO_2 crystallites during high-temperature oxidative treatments. UV–visible and X-ray absorption spectroscopic studies of precursor and oxidized samples suggest that oxyhydroxide surfaces lead to dispersed WO_x species (<7.9 wt.% W) after initial contact with aqueous metatungstate solutions and drying at 400 K. X-ray absorption spectra at the W-L_1 edge show the predominant presence of distorted octahedral species similar those in bulk WO_3 at all WO_x surface densities. The growth of WO_x domains as WO_x surface density increases was detected by a decrease in the absorption edge energies measured by UV–visible spectroscopy. Temperature-programmed reduction analysis of WO_x–ZrO_2 samples show marked changes in reduction behavior with increasing WO_x surface density. As the WO_x surface density increases, WO_x species convert from strongly bound WO_x species to two- and three-dimensional structures, which reduce at lower temperatures.

The addition of a metal function (0.3% wt. Pt) increases the turnover rate (based on W atoms) and selectivity for *n*-heptane isomerization. Quasi-equilibrated hydrogen transfer elementary steps during *n*-heptane isomerization reactions decrease the surface residence time of intermediates and lead to desorption of isomers before β-scission events occur on the acid sites. H_2, O_2, and CO chemisorption uptakes indicate that H atoms spillover onto WO_x species forming $W^{6-n}O_x$–(*n*-H^+) Brønsted acid centers under reaction conditions. H atoms formed at H_2 dissociation sites become involved not only in the desorption of adsorbed intermediates, but also in the generation and maintenance of Brønsted acid sites.

Maximum *o*-xylene isomerization turnover rates were found on WO_x domains of intermediate size at WO_x surface densities (10 W nm^{-2}) greater than monolayer coverage on ZrO_2. Turnover rates depend only on the WO_x surface density, and not independently on the oxidation temperature and WO_x concentration used to obtain a specific density. WO_x domains of intermediate size appear to provide a compromise between reducibility and accessibility of these WO_x domains. At low coverages, turnover rates increase with increasing WO_x surface density, which is related to the pronounced ability of the polyoxoanion domains to form $W^{6-n}O_x$–(*n*-H^+) Brønsted acid centers. As WO_x surface density is further increased, W-atom turnover rates decrease because increasing amounts of WO_x species reside inside WO_3 crystallites. H_2 is required during *o*-xylene isomerization reactions on WO_x–ZrO_2 to prevent the occasional desorption of H atoms as H_2, which leads to the destruction of these Brønsted acid sites via the microscopic reverse of the dissociative chemisorption step. These desorption processes lead to the disappearance of Brønsted

acid sites and to the formation of strongly adsorbed unsaturated species that deactivate the catalysts.

ACKNOWLEDGMENTS

The authors acknowledge financial support for this work from the National Science Foundation (CTS-9510575). X-Ray absorption experiments were performed at the Stanford Synchrotron Radiation Laboratory (SSRL) and supported, in part, by the U.S. Department of Energy. We also thank Messrs. W. E. Gates and J. E. Baumgartner of Exxon Research and Engineering Co. for their help with the high-pressure *n*-heptane isomerization and D_2/*n*-heptane exchange experiments.

REFERENCES

1. Thomas, J. M., *Sci. Am*. **266**, 112 (1992).
2. Tanabe, K., Hattori, H., and Yamaguchi, T., *Crit. Rev. Surf. Chem*. **1**, 1 (1990).
3. Arata, K., *Adv. Catal.* **17**, 165 (1990).
4. Holm, V. C. F., and Bailey, G. C., U.S. Patent 3,032,599, 1962.
5. Hollstein, E. J., Wei, J. T., and Hsu, C. Y., Sun Refining and Marketing Co., U.S. Patent 4,918,041, 1990.
6. Iglesia, E., Soled, S. L., and Kramer, G. M., *J. Catal*. **144**, 238 (1993).
7. Ebitani, K., Konishi, J., and Hattori, H., *J. Catal.* **130**, 257 (1991).
8. Hosoi, T., Shimidzu, T., Itoh, S., Baba, S., Takaoka, H., Imai, T., and Yokoyama, N., *Prepr. Am. Chem. Soc. Div. Pet. Chem*. **33**, 562 (1988).
9. Misono, M., *Catal. Rev. Sci. Eng.* **29**, 269 (1987).
10. Ribeiro, F. H., Boudart, M., Dalla-Betta, R. A., and Iglesia, E., *J. Catal*. **130**, 498 (1991).
11. Soled, S. L., McVicker, G. B., Murrell, L. L., Sherman, L. G., Dispenziere, N. C., Hsu, S. L., and Waldman, D., *J. Catal.* **111**, 286 (1988).
12. Arata, K., and Hino, M., *in* "Proceedings, 9th International Congress on Catalysis, Calgary, 1988" (M. J. Phillips and M. Ternan, Eds.), p. 1727. Chem. Institute of Canada, Ottawa, 1988.
13. Hino, M., and Arata, K., *Chem. Lett.*, 971 (1989).
14. Soled, S. L., Dispenziere, N., and Saleh, R., *in* "Progress in Catalysis" (K. J. Smith and E. C. Sanford, Eds.), p. 77. Elsevier, Amsterdam, 1992.
15. Chang, C. D., Santiesteban, J. G., and Stern, D. L., Mobil Oil Corp., U.S. Patent 5,345,026, 1994.
16. Iglesia, E., Barton, D. G., Soled, S. L., Miseo, S., Baumgartner, J. E., and Gates, W. E., *in* "Proc. 14th North American Meeting Catal. Soc." 1995.
17. Iglesia, E., Barton, D. G., Soled, S. L., Miseo, S., Baumgartner, J. E., and Gates, W. E., *in* Abstracts, 1995 Spring Meeting, American Chemical Society.
18. Iglesia, E., Barton, D. G., Soled, S. L., Miseo, S., Baumgartner, J. E., Gates, W. E., Fuentes, G. A., and Meitzner, G. D., *Stud. Surf. Sci. Catal.* **101**, 533 (1996).
19. Larsen, G., Lotero, E., and Parra, R. D., *Stud. Surf. Sci. Catal.* **101**, 543 (1996).
20. Hino, M., and Arata, K., *J. Chem. Soc. Chem. Commun.*, 1259 (1987).
21. Farcasiu, D., Ghenciu, A., and Miller, G. J., *J. Catal.* **134**, 118 (1992).
22. Soled, S. L., Miseo, S., Baumgartner, J. E., Gates, W. E., Barton, D. G., and Iglesia, E., *in* "Proc. 13th Int. Conf. Catal.," p. 17. 1994.
23. Pines, H., "The Chemistry of Catalytic Hydrocarbon Conversions." Academic Press, New York, 1981.
24. Iglesia, E., Baumgartner, J. E., Ribeiro, F. H., and Boudart, M., *J. Catal.* **131**, 523 (1991).
25. Rijnten, H. T., Ph.D. thesis, Delft University of Technology, 1971.
26. Crucean, E., and B., R., *Trans. J. Brit. Ceram. Soc.* **78**, 58 (1979).
27. Gimblett, F. G. R., Rahman, A. A., and Sing, K. S. W., *J. Colloid Interface Sci.* **84**, 337 (1981).
28. Smith, J. M., "Chemical Engineering Kinetics," 2nd ed. McGraw–Hill, New York, 1970.
29. Schreiner, W. N., and Jenkins, R., *Adv. X-Ray Anal.* **26**, 141 (1983).
30. Toraya, H., Yoshimura, M., and Somiya, S., *J. Am. Ceram. Soc.* **67**, C (1984).
31. Klug, H. P., and Alexander, L. E., "X-Ray Diffraction Procedures." Wiley, New York, 1974.
32. Sayers, D. E., Lytle, F. W., and Stern, E. A., *Phys. Rev. Lett.* **27**, 1204 (1971).
33. Meitzner, G., and Sinfelt, J. H., *Catal. Lett.* **30**, 1 (1995).
34. Iglesia, E., Baumgartner, J. E., Price, G. L., Rose, K. D., and Robbins, J. L., *J. Catal.* **125**, 95 (1990).
35. Price, G. L., and Iglesia, E., *Ind. Eng. Chem*. **28**, 839 (1989).
36. Garvie, R. C., and Goss, M. F., *J. Mater. Sci.* **21**, 1253 (1986).
37. Norman, C. J., *Catal. Today* **20**, 313 (1994).
38. Yamaguchi, T., *Catal. Today* **20**, 199 (1994).
39. Mercera, P. D. L., Van Ommen, J. G., Doesburg, E. B. M., Burggraaf, A. J., and Ross, J. R. H., *Appl. Catal.* **71**, 363 (1991).
40. Srinivasan, R., Keogh, R. A., Milburn, D. R., and Davis, B. H., *J. Catal.* **153**, 123 (1995).
41. McCullough, J. D., and Trueblood, K. N., *Acta Crystallogr.* **12**, 507 (1959).
42. Fuentes, G. A., unpublished results.
43. German, R. M., "Sintering Theory and Practice." Wiley, New York, 1996.
44. Wachs, I. E., "Characterization of Catalytic Materials." Butterworth–Heinnemann, Boston, 1992.
45. Regalbuto, J., *Catal. Lett.* **29**, 189 (1994).
46. Vermaire, D. C., and van Berge, P. C., *J. Catal.* **116**, 309 (1989).
47. Pope, M. T., "Heteropoly and Isopoly Oxometallates." Springer-Verlag, Berlin, 1983.
48. Shadle, E., Hedman, B., Hodgson, K. O., and Solomon, E. I., *Inorg. Chem*. **33**, 4235 (1994).
49. Li, P., and Chen, I. W., *J. Am. Ceram. Soc.* **77**, 118 (1994).
50. Horsley, J. A., Wachs, I. E., Brown, J. M., Via, G. H., and Hardcastle, F. D., *J. Phys. Chem*. **91**, 4014 (1987).
51. Hilbrig, F., Gobel, H. E., Knozinger, H., Schmelz, H., and Lengeler, B., *J. Phys. Chem*. **95**, 6973 (1991).
52. Loopstra, O., and Boldrini, P., *Acta Crystallogr.* **21**, 158 (1966).
53. Haller, G. L., and Resasco, D. E., *Adv. Catal.* **36**, 173 (1989).
54. Ebitani, K., Tsuji, J., Hattori, H., and Kita, K., *J. Catal.* **135**, 609 (1992).
55. Cortes, A., and Corma, A., *J. Catal.* **51**, 338 (1978).
56. Morin, S., Gnep, N. S., and Guisnet, M., *J. Catal.* **159**, 296 (1996).
57. Taylor, W. J., Wagman, D. D., Williams, M. G., Pitzer, K. S., and Rossini, F. D., *J. Res. Natl. Bur. Std.* **37**, 95 (1946).
58. Santiesteban, J. G., Vartuli, J. C., Han, S., Bastian, R. D., and Chang, C. D., *J. Catal.* **168**, 431 (1997).
59. Granqvist, C. G., "Handbook of Inorganic Electrochromic Materials." Elsevier, Amsterdam, 1995.
60. Weber, R. S., *J. Catal.* **151**, 470 (1995).